

Magnetic properties and domain structure of ultrathin yttrium iron garnet/Pt bilayers

J. Mendil,¹ M. Trassin,¹ Q. Bu,¹ J. Schaab,¹ M. Baumgartner,¹ C. Murer,¹ P. T. Dao,¹ J. Vijayakumar,² D. Bracher,² C. Bouillet,³ C. A. F. Vaz,² M. Fiebig,¹ and P. Gambardella¹

¹*Department of Materials, ETH Zurich, CH-8093 Zurich, Switzerland*

²*Swiss Light Source, Paul Scherrer Institut, CH-5232 Villigen PSI, Switzerland*

³*Institut de Physique et Chimie des Matériaux de Strasbourg (IPCMS), UMR 7504 CNRS, Université de Strasbourg, 67034 Strasbourg, France*

(Dated: March 21, 2019)

We report on the structure, magnetization, magnetic anisotropy, and domain morphology of ultrathin yttrium iron garnet (YIG)/Pt films with thickness ranging from 3 to 90 nm. We find that the saturation magnetization is close to the bulk value in the thickest films and decreases towards low thickness with a strong reduction below 10 nm. We characterize the magnetic anisotropy by measuring the transverse spin Hall magnetoresistance as a function of applied field. Our results reveal strong easy plane anisotropy fields of the order of 50-100 mT, which add to the demagnetizing field, as well as weaker in-plane uniaxial anisotropy ranging from 10 to 100 μ T. The in-plane easy axis direction changes with thickness, but presents also significant fluctuations among samples with the same thickness grown on the same substrate. X-ray photoelectron emission microscopy reveals the formation of zigzag magnetic domains in YIG films thicker than 10 nm, which have dimensions larger than several 100 μ m and are separated by achiral Néel-type domain walls. Smaller domains characterized by interspersed elongated features are found in YIG films thinner than 10 nm.

I. INTRODUCTION

Yttrium iron garnet (YIG) thin films have attracted considerable interest in the field of spintronics due to the possibility of converting magnon excitations into spin and charge currents flowing in an adjacent nonmagnetic metal (NM) layer. Spin currents in YIG/NM bilayers have been excited thermally (spin Seebeck effect)¹⁻⁴, dynamically (spin-pumping)⁵⁻⁸ or by means of the spin Hall effect⁹⁻¹³. In the latter case, a charge current in the NM generates a transverse spin current that is either absorbed or reflected at the interface with YIG. This leads to a variety of interesting effects such as the spin Hall magnetoresistance¹⁴⁻¹⁷ (SMR) and current-induced spin-orbit torques¹⁸⁻²⁰, which can be used to sense and manipulate the magnetization. For the latter purpose, it is desirable to work with thin magnetic films in order to achieve the largest effect from the interfacial torques.

For a long time, the growth of YIG has been accomplished by liquid phase epitaxy, which offers excellent epitaxial quality and dynamic properties such as low damping and a rich spin-wave spectrum. The magnetic properties of these bulk-like samples, including the magnetocrystalline anisotropy^{21,22} and magnetic domain structure²³⁻²⁵, have been extensively characterized in the past. However, with rare exceptions²⁶, samples grown by liquid phase epitaxy usually have thicknesses in the μ m to mm range. Recent developments in oxide thin film growth give access to the sub- μ m range by employing techniques such as laser molecular beam epitaxy²⁷, sputtering^{28,29}, and pulsed laser deposition (PLD)³⁰⁻³⁷, which allow for growing good quality films with thickness down to the sub-100-nm range^{28,29,35-37} and even below 10 nm^{27,33,34}. Since the thickness as well as structural

and compositional effects have a large influence on the magnetic behavior, these developments call for a detailed characterization of the magnetic properties of ultrathin YIG films. Several characteristic quantities, which are of high relevance for YIG-based spintronics, have been found to vary in films thinner than 100 nm. For instance, a reduction of the saturation magnetization^{29,35-40} is typically observed in YIG films with thickness down to 10 nm, which has been ascribed to either thermally-induced stress³⁸, lack of exchange interaction partners at the interface³⁶, or stoichiometric variations^{29,37,39,40}. Furthermore, an increase of the damping^{33-35,41} as well as a decreased spin mixing conductance^{42,43} have been found in ultrathin YIG. Finally, the emergence of unexpected magnetocrystalline anisotropy was reported for films of different orientations grown on gadolinium gallium garnet (GGG) and yttrium aluminium garnet (YAG). The magnetic anisotropy was investigated by the magneto-optical Kerr effect in GGG/YIG(111)^{27,36} and by ferromagnetic resonance in GGG/YIG(111)³¹, GGG/YIG(001)³², and YAG/YIG(001)²⁸. Whereas all these studies address important magnetic characteristics in the sub-100 nm range, only few studies^{33,34} explore the ultrathin film regime below 10 nm. This thickness range is highly relevant for efficient magnetization manipulation using current-induced interfacial effects as well as for strain engineering, since strain and its gradients relax after 10 to 20 nm. Finally, a comprehensive knowledge of the domain and domain wall structure in the thin film regime is lacking. Recent studies on magnetic domains address only bulk²⁵, several micrometers⁴⁴ or hundreds of nanometers⁴⁵ thick YIG films.

In this work, we present a systematic investigation of the structure, saturation magnetization, magnetic anisotropy, and magnetic domains of YIG/Pt films grown

on GGG substrates by PLD as a function of YIG thickness from $t_{\text{YIG}} = 3.4$ to $t_{\text{YIG}} = 90$ nm. By combining x-ray diffraction (XRD), transmission electron microscopy (TEM), atomic force microscopy (AFM) and x-ray absorption spectroscopy, we show that our films possess high crystalline quality and smooth surfaces with no detectable interface mixing throughout the entire thickness range. The saturation magnetization, investigated using a superconducting quantum interference device (SQUID), shows values close to bulk for thick films and a gradual reduction towards lower thicknesses. We probe the magnetic anisotropy electrically by means of SMR and find an easy plane and uniaxial in-plane anisotropy with a non-monotonic variation of the in-plane orientation of the easy axis and the magnitude of the effective anisotropy field. Finally, we investigate the domain structure using x-ray photoelectron emission microscopy (XPEEM), evidencing significant changes in the domain structure above and below $t_{\text{YIG}} = 10$ nm. Our results provide a basis for understanding the behavior of spintronic devices based on YIG/Pt with different YIG thickness.

II. GROWTH AND STRUCTURE

We prepared three sample series consisting of GGG/YIG(t_{YIG})/Pt bilayers with Pt thickness set to 3 nm in the first two series for optimal SMR measurements and 1.9 nm in the third series to allow for surface-sensitive XPEEM measurements while avoiding charging effects. The YIG thickness, t_{YIG} , varies from 3.4 to 90 nm. An overview of the samples and their thickness in nm and YIG unit cells can be found in Table I. The samples have been grown in-situ on (111)-oriented GGG substrates using an ultra-high vacuum PLD system combined with dc magnetron sputtering (base pressure 10^{-8} mbar, 10^{-10} mbar, respectively). The YIG was grown by PLD at a growth pressure of 10^{-1} mbar and temperature of 720 °C using an excimer KrF laser (wavelength 248 nm) at a repetition rate of 8 Hz and 1.45 J/cm² fluence. Reflection high energy electron diffraction (RHEED) was used to monitor the growth rate in-situ. After cooling down under a 200 mbar O₂ atmosphere, the GGG/YIG films were transferred to the sputtering chamber without breaking the ultra-high vacuum, where Pt was deposited at room temperature under 10^{-2} mbar Ar pressure. Finally, for electrical transport measurements, the YIG(t_{YIG})/Pt(3) series were patterned into Hall bar structures using optical lithography followed by Ar-ion milling. The Hall bars are oriented parallel to the $[1\bar{1}0]$ crystal direction and are 50 μm wide, with a separation of the Hall arms of 500 μm .

The crystalline quality and epitaxial strain of the GGG/YIG(111) films were investigated using XRD to obtain $\theta - 2\theta$ diffraction scans and reciprocal space maps. The interface quality was probed using scanning TEM (STEM), energy dispersive x-ray spectroscopy (EDS),

	t_{Pt} [nm]	t_{YIG} [nm, (unit cells)]						
SMR 1	3	3.4,	4.6,	6.2,	7.3,	9,	29,	90
		(2.7)	(3.7)	(5.0)	(5.9)	(7.3)	(23.4)	(72.7)
SMR 2	3	3.7,	5.6,	6.2,	6.8,	7.4,	12.4	
		(3.0)	(4.5)	(5.0)	(5.5)	(6.0)	(10.0)	
XPEEM	1.9	3.7,	8.7,	12.4,	28.5,	86.7		
		(3.0)	(7.0)	(10.0)	(23.0)	(70.0)		

TABLE I. Overview of the three sample series used for anisotropy characterization using SMR and domain structure using XPEEM where t_{Pt} and t_{YIG} refer to the Pt and YIG thickness, respectively. The numbers between parentheses refer to the thickness in unit cells of YIG (1 unit cell=1.238 nm [46]).

and electron energy loss spectroscopy (EELS) in order to resolve the elemental composition, whereas the thin film topography was investigated using AFM in both contact and tapping mode.

The YIG films are single phase epitaxial layers with (111) orientation, as indicated by the diffraction peaks corresponding to the (111) planes in the diffraction pattern. The x-ray diffractograms for three selected YIG thicknesses are shown in Fig. 1 (a-c). Kiessig thickness fringes indicate the homogeneous growth and high interface quality. The observed periodicity matches the thicknesses determined by x-ray reflectivity. To further investigate the crystalline quality and the interfacial strain states of the YIG films, we recorded reciprocal space maps around the (664) and (486) diffractions for both YIG and the GGG substrate. These maps allow us to probe the strain state of the films along the two inequivalent $[11\bar{2}]$ and $[1\bar{1}0]$ in-plane directions. A coherent strain state of the films was evidenced for all thicknesses considered. The good lattice matching between YIG and GGG results in high quality epitaxial growth and no detectable strain relaxation, as shown by the alignment of the diffraction points along both $[11\bar{2}]$ and $[1\bar{1}0]$ orientations. The reciprocal space maps measured on a 99 nm-thick YIG film are shown in Fig. 1 (d) and (e).

Figures 1 (f,g) show high resolution STEM images of the two interfaces and a TEM image of the full stack in the inset. The corresponding chemical profiles across the interfaces probed by EDS are shown in Figs. 1 (h,j). The EDS profiles indicate a moderate interdiffusion of Fe, Y, and Pt within a range of 2 nm at the YIG/Pt interface and of Gd and Ga into YIG within a range of about 4 nm at the GGG/YIG interface. Both values are in agreement with recent findings^{39,47}. The smaller diffusion range at the YIG/Pt interface is consistent with the low power and lower deposition temperature (room temperature) of Pt compared to the deposition of YIG on GGG. The moderate diffusion of Ga and Gd into the YIG film is also in agreement with previous reports^{29,39}. The EELS analysis, shown in Fig. 2, confirms the moderate diffusion of Fe in the Pt. In order to gain information on the evolution of the local Fe environment across the

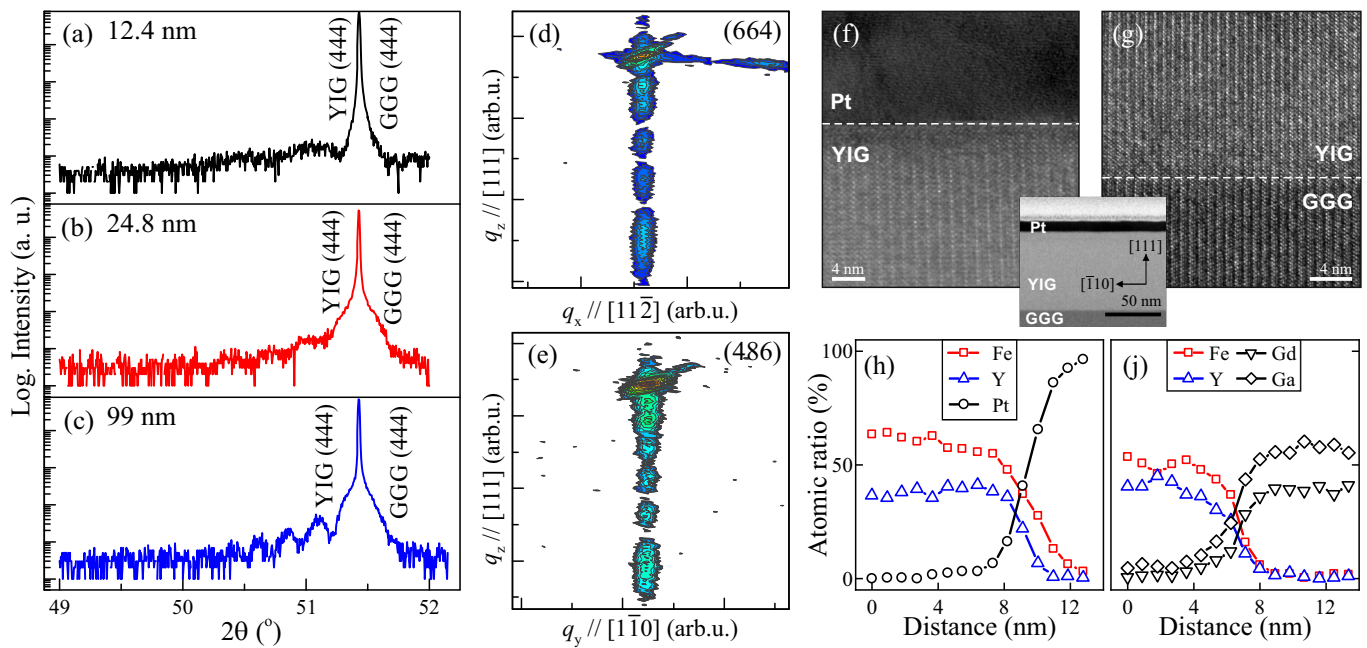


FIG. 1. (a-c) Structural characterization of GGG/YIG(111) films of different thickness by $\theta - 2\theta$ scans using XRD. (d,e) Reciprocal space maps around the (664) and (486) diffraction peaks. The oscillations in the $\theta - 2\theta$ and q_z scans are thickness oscillations. The thickness derived from these measurements agrees with that measured using XRD. (f,g) High resolution STEM image of the two interfaces in the stack GGG/YIG(72)/Pt(9). The inset shows a cross-section of the full stack. (h,j) Elemental profiles across the YIG/Pt and YIG/GGG interfaces measured by EDS.

YIG/Pt interface, we calculated the intensity ratio of the Fe L_3 and L_2 white lines from the Fe EELS spectra measured within the YIG film (black dot in Fig. 2) and at two different positions near the YIG/Pt interface (red and blue dots). In YIG, the L_3/L_2 ratio is 5.64, which is consistent with an Fe^{3+} oxidation state, as found, e.g., in Fe_2O_3 (Ref. 48). On the Pt side of the YIG/Pt interface, the L_3/L_2 ratio decreases to 4.24, which is in between the values found for Fe and FeO. This change of electronic valence confirms the presence of Fe in the interfacial Pt layer. We note that the absence of Fe^{3+} in the Pt further excludes measurement artifacts due to sample preparation for TEM, such as Pt redeposition

The AFM measurements substantiate the low roughness expected from the x-ray reflectivity and the observation of Kiessig fringes in the diffraction spectra. Figure 3 (a) shows an AFM image over an area of $3 \times 3 \mu\text{m}^2$ of a 28.5 nm thick GGG/YIG film. The measured roughness is in the range of 1 Å and is independent of the YIG thickness, as shown in Fig. 3 (b).

III. SATURATION MAGNETIZATION

Figure 4 (a) shows the saturation magnetization (M_s) of the unpatterned YIG(t_{YIG})/Pt(3) bilayers measured by SQUID (sample series SMR 1 and SMR 2 in red and grey, respectively). For each thickness, we observe a hysteretic in-plane magnetization with coercivity smaller

than 0.5 mT, as illustrated for YIG(9)/Pt(3) in Fig. 4 (b). The thickest sample, YIG(90)/Pt(3), has a saturation magnetization of $\mu_0 M_s = 153$ mT, which is close to the bulk value of $\mu_0 M_{s,\text{bulk}} = 180$ mT at room temperature.⁴⁹ The reduction of M_s compared to the bulk was also observed in other studies of YIG films grown by PLD^{31,36,50,51}. This reduction has been ascribed to the different percentage of Fe vacancies at the tetrahedral or octahedral sites³¹, the lack of exchange

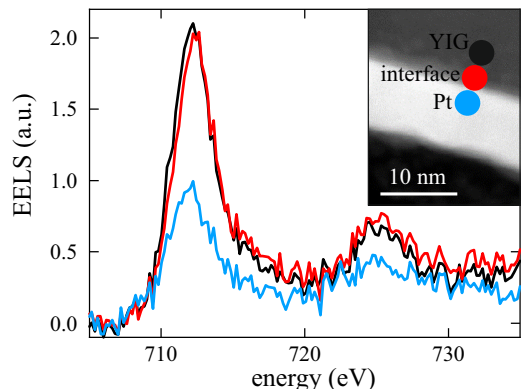


FIG. 2. Comparison of the Fe $L_{2,3}$ spectra measured by EELS across the YIG/Pt interface. The spectra, shown after background subtraction, have been averaged on 3 nm-long line scans for each region of interest, as labeled in the inset with colored dots. The probe beam diameter is 0.15 nm.

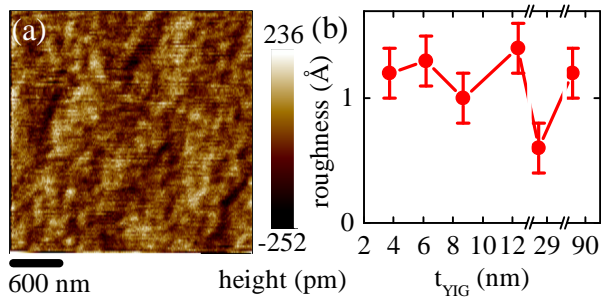


FIG. 3. (a) AFM image of YIG(28.5)/Pt(3). (b) Root mean square roughness as a function of YIG thickness measured by AFM.

interaction partners for atoms at the interface³⁶, strain relaxation due to a slight lattice mismatch of the substrate and YIG⁵⁰, as well as to the presence of Fe and O vacancies⁵¹. Furthermore, we observe a decreasing trend for M_s at lower YIG thicknesses, with a steeper reduction below 10 nm. Our thinnest sample ($t_{\text{YIG}} = 3.4$ nm) has $\mu_0 M_s = 27$ mT, which is only 15% of the bulk saturation magnetization. Previous studies reported a decreasing trend of M_s already for thicknesses larger than 10 nm (Refs. 29, 36, 39, 40, and 50).

The reduction of the YIG magnetization in thin films has been often modeled as a magnetically dead layer. For example, by extrapolating the areal magnetization as a function of thickness to the point where no surface magnetization would be present, Mitra et al.³⁹ inferred a 6 nm thick dead layer for YIG films in the 10-50 nm thickness range. A similar extrapolation of our M_s data for samples with thickness of 9 nm and above would lead to a 4.3 nm thick dead layer. However, our data evidence a finite magnetization below 4.3 nm, contradicting the assumption of an abrupt magnetically dead layer at the GGG/YIG interface. Instead, we conclude that a gradual reduction of M_s occurs at thicknesses below 10 nm, which may be due to the diffusion of Gd from the GGG substrate into YIG observed by EDS [see Fig. 1 (j)].

Further information on the magnetization of YIG(t_{YIG})/Pt(1.9) was obtained using x-ray absorption spectroscopy and x-ray magnetic circular dichroism (XMCD) at the L_3 and L_2 absorption edges of Fe. The x-ray absorption spectra of representative YIG(3.7,12.4,86.7)/Pt(1.9) samples present a very similar lineshape [Fig. 4 (c)], which implies that the chemical environment of the Fe atoms does not change substantially with thickness. The XMCD asymmetry, however, decreases in the thinner samples [Fig. 4 (d)], consistent with the behavior of M_s discussed above. These data confirm that our samples are magnetic throughout the entire thickness range and suggest that the reduction of M_s is not due to defective Fe sites.

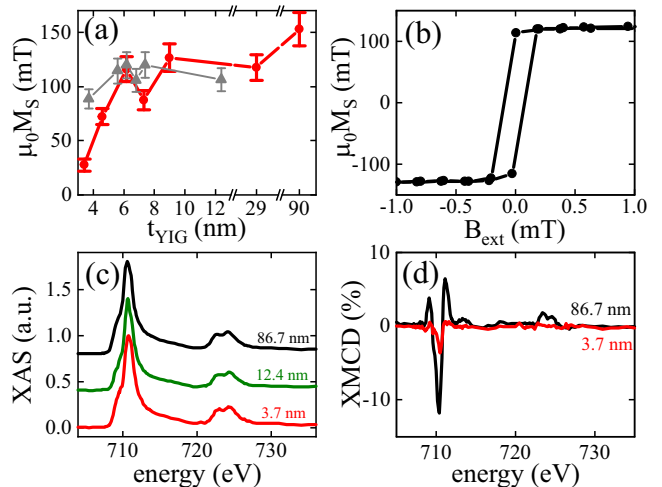


FIG. 4. (a) M_s as a function of YIG thickness measured by SQUID for sample series SMR 1 (red) and SMR 2 (grey). (b) Magnetic hysteresis of YIG(9)/Pt(3) as a function of in-plane magnetic field. (c) X-ray absorption spectra of YIG(3.7,12.4,86.7)/Pt(1.9). Each line represents the sum of two spectra acquired with positive and negative circular x-ray polarization. The spectra are shifted by a constant offset for better visibility. (d) XMCD spectra for the thickest and thinnest samples obtained by taking the difference between two absorption spectra acquired with positive and negative circular x-ray polarization. The spectra were acquired on homogeneously magnetized domains in the XPEEM setup.

IV. MAGNETIC ANISOTROPY

To probe the magnetic anisotropy, we performed measurements of the transverse SMR^{14,15} as a function of magnitude and orientation of the external magnetic field B_{ext} . Our data evidence the presence of an easy-plane anisotropy field, B_{K_1} , which adds to the demagnetization field to favor the in-plane magnetization, as well as of an easy axis field B_{K_2} , which favors a particular in-plane direction that varies from sample to sample.

A. Transverse SMR measurements

A sketch of the Hall bar structure employed for the SMR measurements is presented in Fig. 5 (a). We used an ac current $I = I_0 \sin(\omega t)$, modulated at a frequency $\omega/2\pi = 10$ Hz, and acquired the longitudinal and transverse (Hall) resistances^{52,53}. To extract the magnetization orientation, we consider here only the transverse resistance, R_{xy} , which is sensitive to all three Cartesian components of the magnetization due to the SMR effect¹⁵. We performed two types of measurements. In the first type, which we call IP angle scan, we vary the in-plane angle of the applied magnetic field B_{ext} ; in the second type, which we call OOP field scan, we ramp B_{ext} applied out-of-plane. For both cases, it is convenient to use spherical coordinates: we define φ_B as the azimuthal

angle between B_{ext} and I and φ as the azimuthal angle between the magnetization and I , whereas the polar angles of B_{ext} and the magnetization with respect to the surface normal are θ_B and θ , respectively [Fig. 5 (a)].

In the IP angle scan ($\theta = \pi/2$), R_{xy} is determined solely by the planar Hall-like (PHE) contribution from the SMR, leading to

$$R_{xy} = R_{\text{PHE}} \sin(2\varphi), \quad (1)$$

where R_{PHE} is the planar Hall-like coefficient. In this type of experiment, we record R_{xy} as a function of φ_B for different B_{ext} . For fields large enough to saturate the magnetization along the field direction, we can assume $\varphi = \varphi_B$ and hence $R_{xy} = R_{\text{PHE}} \sin(2\varphi_B)$. Conversely, for external fields small enough such that $\varphi \neq \varphi_B$, R_{xy} will deviate from the $\sin(2\varphi_B)$ curve. By adopting a macrospin model assuming in-plane uniaxial magnetic anisotropy and comparing the resulting PHE from Eq. (1) with our data, we can determine quite accurately the easy axis direction as well as the magnitude of the in-plane magnetic anisotropy energy.

In the OOP field scans, R_{xy} depends on the ordinary Hall effect (OHE) and anomalous Hall-like (AHE) contribution from the SMR, which is proportional to the out-of-plane component of magnetization¹⁵. We thus have

$$R_{xy} = R_{\text{OHE}} B_{\text{ext}} \cos \theta_B + R_{\text{AHE}} \cos \theta, \quad (2)$$

where R_{OHE} and R_{AHE} are the OHE and AHE coefficients, respectively. When ramping the OOP field, the contribution due to R_{OHE} continuously increases, whereas the contribution due to R_{AHE} saturates as the magnetization is fully aligned out-of-plane. The corresponding saturation field B_s can be used to determine the out-of-plane magnetic anisotropy knowing the value of M_s . All measurements were performed at room temperature using a current density in the low 10^5 A/cm² range.

B. Easy plane anisotropy

The easy-plane anisotropy field was determined by comparing the hard axis (out-of-plane) saturation field B_s measured by the Hall resistance with the demagnetizing field $\mu_0 M_s$ estimated using SQUID. Figures 5 (b) and (c) show the results of OOP field scans for the thickest (90 nm) and thinnest (3.4 nm) YIG/Pt(3) samples. In both cases, we identify B_s (dashed line) as the field above which only the ordinary Hall effect contributes to the (linear) increase of R_{xy} with increasing field. Note that, for YIG(90)/Pt(3), we observe a bell-shaped curve that is due to the PHE during the re-orientation of magnetic domains from the initial in-plane to the final out-of-plane orientation at B_s . Figure 5 (d) reports the estimated values of B_s for all thicknesses. In all cases, we find that B_s is significantly larger than $\mu_0 M_s$ reported in Fig. 4 (a). We attribute this difference to an easy-plane anisotropy

field, $B_{K_1} = B_s - \mu_0 M_s$, which favors in-plane magnetization. The magnitude of B_{K_1} varies in the range of 50-

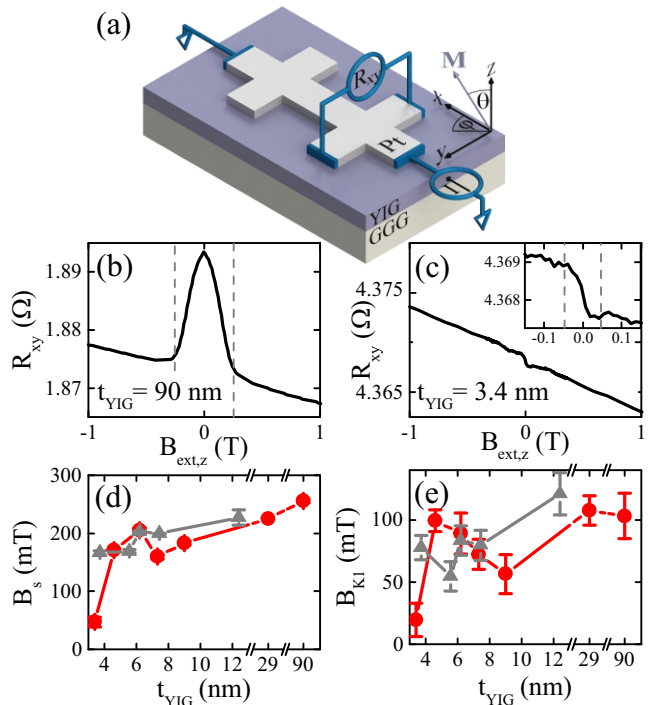


FIG. 5. (a) Schematic of the Hall bar and coordinate system. OOP field scans for the thickest (90 nm) and thinnest (3.4 nm) YIG thickness from series SMR 1 are shown in (b) and (c), respectively. From these scans, the out-of-plane saturation field B_s was determined as indicated by the dashed line and summarized in (d) as a function of YIG thickness. (e) Easy-plane anisotropy field $B_{K_1} = B_s - \mu_0 M_s$. Data shown for sample series SMR 1 (red) and SMR 2 (grey).

100 mT (except for the thinnest sample). This additional easy plane anisotropy is of the same order of magnitude as in previous studies^{27,36}, where it was attributed to a rhombohedral unit cell distortion along the [111] direction by ≈ 1 %. Interestingly, the thinnest sample shows a drastically reduced B_{K_1} compared to the thicker ones, suggesting that very thin YIG films with $t_{\text{YIG}} \leq 3.4$ nm tend to develop out-of-plane magnetic anisotropy³⁸. This tendency, however, is not sufficient to induce an out-of-plane easy axis, as verified by SQUID measurements as a function of out-of-plane field. The reduction of B_{K_1} may also explain the absence of the bell-shaped PHE contribution to R_{xy} observed in Fig. 5 (c).

C. In-plane uniaxial anisotropy

The in-plane uniaxial anisotropy field B_{K_2} is determined by measuring IP angle scans of R_{xy} for different constant values of B_{ext} . By choosing B_{ext} below the in-plane saturation field and fitting R_{xy} as a function of φ_B using a macrospin model, we determine the orientation of the in-plane easy axis as well as the magnitude of B_{K_2} .

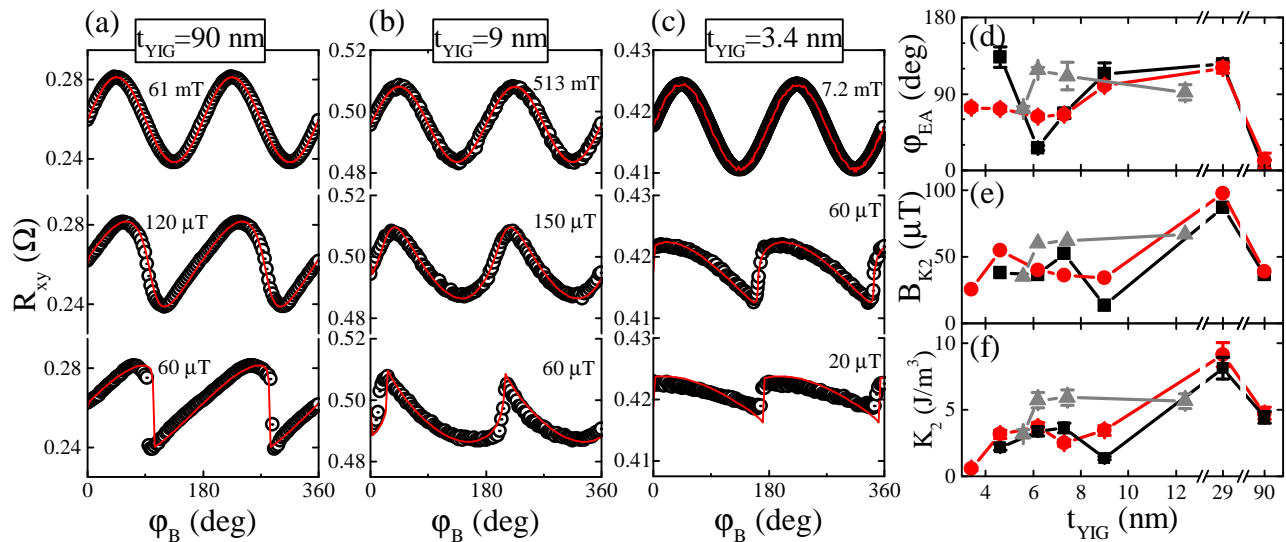


FIG. 6. Transverse resistance R_{xy} as a function of azimuthal orientation of the external magnetic field, φ_B , for different thicknesses in (a-c). The data are shown by black symbols, the macrospin simulations by red solid lines. (d) Easy axis orientation, φ_{EA} , relative to the $[1\bar{1}0]$ crystal axis. (e) Effective uniaxial anisotropy field B_{K_2} and (f) in-plane uniaxial energy $M_s B_{K_2}$ as a function of YIG thickness. Black and red points show the results for two different Hall bars patterned on the same chips of series SMR 1; grey triangles are results obtained on Hall bars of series SMR 2.

The black circles in Fig. 6 (a-c) show R_{xy} as a function of φ_B for three representative YIG thicknesses (90, 9, 3.4 nm). For all three samples, we identify the $\sin(2\varphi)$ behavior expected from Eq. (1) for $B_{\text{ext}} > 7.2$ mT [upper panels in Fig. 6 (a-c)]. When reducing B_{ext} , deviations from this lineshape occur, indicating that the magnetization no longer follows the external magnetic field. This behavior is most pronounced for fields of only tens of μT [lower panels in Fig. 6 (a-c)]. For such low fields, we observe two prominent jumps of R_{xy} separated by 180° , which we attribute to the magnetization switching abruptly from one quadrant to the opposite one during an IP angle scan in proximity to the hard axis. These jumps, which occur at different φ_B for the three samples, indicate the presence of in-plane uniaxial anisotropy.

In order to quantify the in-plane uniaxial anisotropy, we perform macrospin simulations of R_{xy} assuming the following energy functional

$$E = -M_s \vec{m} \cdot \vec{B}_{\text{ext}} + M_s B_{K_2} \sin^2(\varphi - \varphi_{\text{EA}}), \quad (3)$$

where \vec{m} is the magnetization unit vector and φ_{EA} defines the angle of the easy axis with respect to the $[1\bar{1}0]$ crystal axis. Expressing \vec{m} and \vec{B}_{ext} in spherical coordinates, i.e., $\vec{m} = (\sin \theta \cos \varphi, \sin \theta \sin \varphi, \cos \theta)$ and $\vec{B}_{\text{ext}} = B_{\text{ext}} (\sin \theta_B \cos \varphi_B, \sin \theta_B \sin \varphi_B, \cos \theta_B)$, and taking $\theta = \theta_B = \pi/2$, we can calculate the equilibrium position of the magnetization as a function of B_{ext} , φ_B , B_{K_2} , and φ_{EA} . This calculation results in a set of values $\varphi(\varphi_B)$ that can be used to simulate R_{xy} using Eq. (1). The planar Hall constants R_{PHE} required for the simulations are obtained by fitting Eq. (1) to the saturated data sets. Finally, we fit $R_{xy}(\varphi_B)$ keeping B_{K_2} and φ_{EA} as free parameters. The fits, shown as red lines in Fig. 6

(a-c), reproduce the main features (lineshape and jumps) of R_{xy} quite accurately, indicating that our method is appropriate to measure weak anisotropy fields in YIG. The resulting values of φ_{EA} and B_{K_2} are shown by the symbols in Fig. 6 (d) and (e), respectively.

The data for the series SMR 1 (red) in Fig. 6 (d) appear to follow a pattern in the orientation of the easy axis as a function of thickness. Very thin samples with $t_{\text{YIG}} \leq 7.2$ nm have $\varphi_{\text{EA}} \approx 60^\circ$, whereas intermediate thicknesses in the range $9 \leq t_{\text{YIG}} \leq 29$ nm have $\varphi_{\text{EA}} \approx 120^\circ$ and the thickest sample, $t_{\text{YIG}} = 90$ nm, has $\varphi_{\text{EA}} \approx 0^\circ$. While these orientations correspond to the three-fold symmetry of the (111) plane, measurements on different sets of samples show that this correspondence is likely coincidental. Measurements performed on devices patterned on the same chip (black squares) of series SMR 1 as well as on one device of the series SMR 2 (grey triangles) reveal uncorrelated variations of φ_{EA} relative to the SMR 1 series, particularly for $t_{\text{YIG}} < 10$ nm. A variation of φ_{EA} for samples grown on the same chip has also been observed in thicker YIG films²⁷ and is most likely due to inhomogeneities of process parameters such as, e.g., the temperature of the sample surface during deposition, which could lead to local strain differences.

Figure 6 (e) shows B_{K_2} as a function of t_{YIG} . Most values are close to $50 \mu\text{T}$, with minima and maxima of about 20 and $100 \mu\text{T}$, respectively. Combined with the thickness-dependent saturation magnetization from Fig. 4 (a), we obtain a magnetic anisotropy energy $K_2 = M_s B_{K_2}$ in the range of 0.1 to $10 \text{ J}/\text{m}^3$ [Fig. 6 (f)]. K_2 is more than two orders of magnitude smaller than the first order cubic anisotropy constant of bulk YIG ($-610 \text{ J}/\text{m}^3$) (Ref. [22]), which reinforces the hypothesis

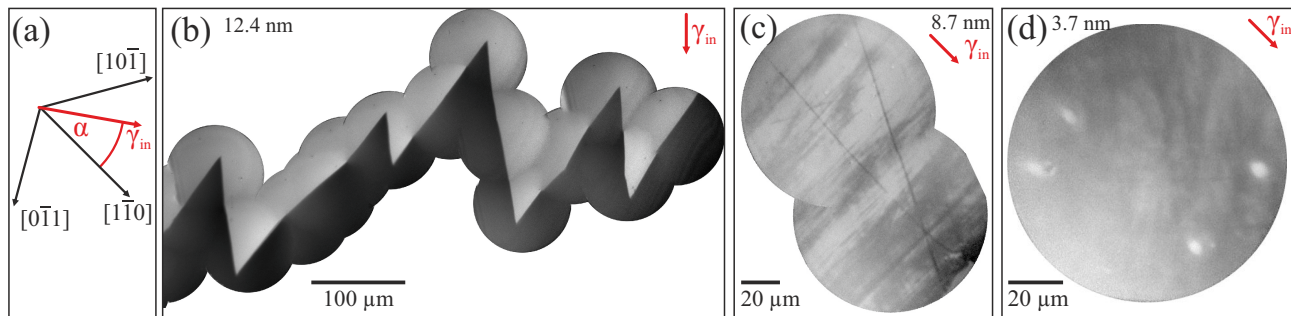


FIG. 7. (a) Schematics of the direction of the incoming x-ray beam (red arrow) relative to the crystal axes in the XPEEM setup. (b-d) Domain structure of YIG/Pt(1.9) bilayers with $t_{\text{YIG}} = 12.4, 8.7,$ and 3.7 nm observed by XPEEM. The gray scale contrast corresponds to different in-plane orientations of the magnetization.

of an extrinsic origin of the uniaxial anisotropy reported here.

Our observation of uniaxial anisotropy agrees with previous studies of YIG films grown by PLD on GGG^{27,31,36,54}. From a crystallographic point of view, however, uniaxial anisotropy is not expected for the YIG(111) plane. Rather, for an ideal (111) crystal plane, one would expect a three-fold anisotropy due to the cubic magnetocrystalline anisotropy of bulk YIG⁵⁵. This becomes obvious when translating the first order magnetocrystalline energy term of cubic crystals ($E_{\text{cubic}} \propto \alpha_1^2 \alpha_2^2 + \alpha_2^2 \alpha_3^2 + \alpha_3^2 \alpha_1^2$, where $\alpha_{1,2,3}$ are the directional cosines with respect to the main crystallographic axes) into the coordinate system of the (111) plane (θ with respect to the [111] direction and, for simplicity, φ with respect to the [112] direction), giving

$$E_{\text{cubic}} \propto \frac{1}{4} \sin^4 \theta + \frac{1}{3} \cos^4 \theta + \frac{\sqrt{2}}{3} \sin^3 \theta \cos \theta \cos 3\varphi. \quad (4)$$

In order for the threefold anisotropy to appear [last term in Eq. (4)], the magnetization has to have a small out-of-plane component ($\theta \neq \pi/2$). Whereas this can be generally guaranteed in bulk crystals, in thin films the demagnetizing field and B_{K_1} force $\theta = \pi/2$, resulting in the absence of threefold cubic anisotropy. The origin of the in-plane uniaxial anisotropy thus remains to be explained. Our XRD measurements reveal no significant in-plane strain anisotropy within the accuracy of the reciprocal space maps in Fig. 1 (d) and (e). The small amplitude of B_{K_2} and the intra- and inter-series variations of φ_{EA} suggest that this anisotropy may originate from local inhomogeneities of the growth or patterning parameters, which should thus be taken into account for the fabrication of YIG-based devices.

V. MAGNETIC DOMAINS

The domain structure in bulk YIG is of flux-closure type with magnetic orientation dictated by the easy axes along the [111]-equivalent directions^{56,57}. In the case of a defect-free YIG crystal, the domains can be as large as

the sample itself, apart from the flux closure domains at the edges. Dislocations and strain favor the formation of smaller domains⁵⁷. External strain and local stress due to dislocations can result in a variety of magnetic configurations such as cylindrical domains⁵⁷ and complex local patterns^{56,58}. Moreover, dislocations serve as pinning sites for domain walls⁵⁹. The domain walls observed at the surface of YIG single crystals are usually of the Bloch type and several μm wide^{56,60}.

In the following, we characterize the domain structure of YIG thin films using XPEEM. The samples are YIG(t_{YIG})/Pt(1.9) bilayers with thickness down to $t_{\text{YIG}} = 3.7$ nm, as described for the XPEEM series in Table I. The measurements were performed at the SIM beamline of the Swiss Light Source⁶¹ by tuning the x-ray energy to obtain the maximum XMCD contrast at the Fe L_3 edge (710 eV) and using a circular field of view with a diameter of 100 μm or 50 μm . Magnetic contrast images were obtained by dividing pixel-wise consecutive images recorded with circular left and right polarized x-rays. Prior to imaging, the samples were demagnetized in an ac magnetic field applied along the surface normal.

A. Domain structure

Figure 7 shows representative XPEEM images of the magnetic domains of 12.4, 8.7, and 3.7 nm thick YIG. Thicker films ($t_{\text{YIG}} = 86.7, 28.5$ and 12.4 nm) present qualitatively similar domain structures such as those shown in Fig. 7 (b) for the 12.4 nm film. The domains in these thicker films extend over hundreds of μm and meet head-on, separated by domain walls with characteristic zigzag boundaries. Such walls are typical of thin films with in-plane uniaxial anisotropy, where the zigzag amplitude and period depends on the balance between magnetostatic charge density and domain wall energy, as well as on the process of domain formation⁶²⁻⁶⁴. Note that the two sides of each zigzag are asymmetric, as found in ion-implanted garnets with uniaxial and trigonal in-plane anisotropy⁶⁵. The length and opening angle of the zigzags increase and decrease, respectively, with

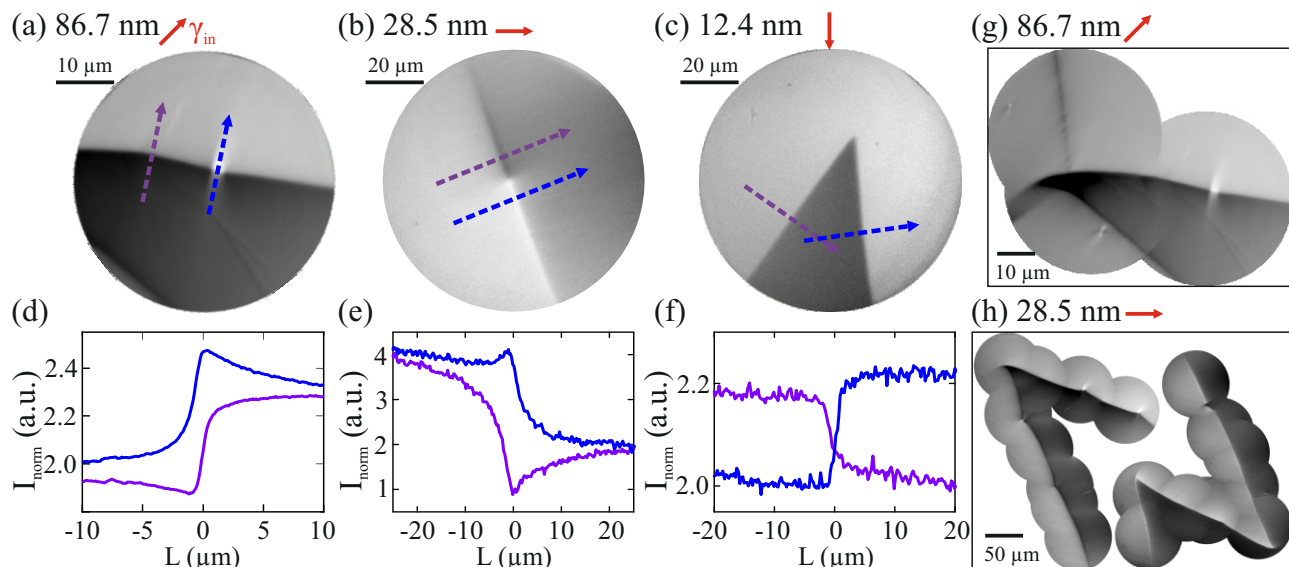


FIG. 8. XPEEM images of domain walls in (a) 86.7 nm, (b) 28.5 nm, and (c) 12.4 nm thick YIG. The arrows indicate the x-ray incidence direction. (d-f) Line profiles of the walls corresponding to the dashed lines in (a-c). (g,h) Details of the apices of the zigzag domains in 86.7 nm and 28.5 nm thick YIG. The samples are oriented with the crystal axes defined in Fig. 7 (a).

increasing film thickness, similar to the trend reported for amorphous Ga-doped Co films with weak uniaxial anisotropy⁶⁵. In a quantitative model based on the mentioned energy balance⁶⁶, both quantities correlate with M_s in a positive and negative manner, respectively. This trend is in agreement with the increase of M_s reported in Fig. 4 (a).

The domain morphology changes abruptly in films thinner than 12.4 nm. YIG films with $t_{\text{YIG}} = 8.7$ and 3.7 nm present much smaller domains, which extend only for tens of μm and have a weaving pattern, as shown in Fig. 7 (c) and (d), respectively. In the 8.7 nm thick film, the domains elongate along the $[11\bar{2}]$ direction, likely due to the presence of in-plane uniaxial anisotropy. In the 3.7 nm thick film, the domains are more irregular and do not present such a strong preferred orientation, consistent with the reduced demagnetizing field and smaller in-plane anisotropy reported for this thickness [see Fig. 5 (e) and 6 (f), respectively].

B. Domain walls

XPEEM images provide sufficient contrast to analyze the domain walls of films with $t_{\text{YIG}} \geq 12.4$ nm, which consist of straight segments along the zigzag boundary shown in Fig. 7 (b). Figures 8 (a-c) show details of the 180° domain walls that delimit the edges of the zigzag domains in 86.7, 28.5 and 12.4 nm thick YIG. Linecuts of the XMCD intensity across the walls are shown in Figs. 8 (d-f). As the XMCD intensity scales with the projection of the magnetization onto the x-ray incidence direction (red arrows), the "overshoot" of the XMCD intensity in the central wall region compared to the side

regions in Figs. 8 (d,e) indicates that the magnetization rotates in the plane of the films. This observation is consistent with the Néel wall configuration expected for thin films with in-plane magnetic anisotropy⁶⁴, and contrasts with the Bloch walls reported at the surface of bulk YIG crystals^{56,60}. The walls appear to have a core region, corresponding to the length over which the magnetic contrast changes most abruptly, which is about 1-2 μm wide, and a tail that extends over several μm , which is a typical feature of Néel walls in soft films with in-plane magnetization⁶⁴.

The domain wall in Fig. 8 (b) shows an inversion of the magnetic contrast at a vortex-like singular point in the middle of the image. Such a contrast inversion reveals that the wall is composed by different segments with opposite rotation mode of the magnetization, i.e., opposite chirality. The singular point that separates two consecutive segments is a so-called Bloch point, which can extend from the top to the bottom of the film, forming a Bloch line. Such features have smaller dimensions compared to the wall width and are therefore considered to favor the pinning of domain walls at defects, thus acting as a source of coercivity in soft magnetic materials⁶⁴.

Figures 8 (g) and (h) further show that the domain walls at the apices of the zigzag domains in the 86.7 and 28.5 nm thick films have a curved shape. This feature suggests that the domains are indeed pinned at defect sites, likely of structural origin^{57,59}. Finally, we note that the domain features reported here move under the influence of an external in-plane magnetic field of the order of few mT, as well as by ramping the out-of-plane field that compensates the magnetic field of the XPEEM lenses at the sample spot.

VI. CONCLUSIONS

Our study shows that the magnetic properties and domain configuration of epitaxial YIG(111) films grown by PLD on GGG and capped by Pt depend strongly on the thickness of the YIG layer. Despite the high structural and interface quality indicated by XRD and TEM, the saturation magnetization decreases from $M_s = 122$ kA/m (15% below bulk value) in 90 nm-thick YIG to 22 kA/m in 3.4 nm-thick YIG. The gradual decrease of M_s suggests a continuous degradation of M_s rather than the formation of a dead layer. All films except the thinner one ($t_{\text{YIG}} = 3.4$ nm) present a rather strong easy-plane anisotropy in addition to the shape anisotropy, of the order of 10^3 to 10^4 J/m³. Additionally, all films except the thinner one present weak in-plane uniaxial anisotropy, of the order of $3 - 10$ J/m³. This anisotropy defines a preferential orientation of the magnetization in each sample, which, however, is found to vary not only as a function of thickness but also between samples with the same nominal thickness and even for samples patterned on the same substrate. The origin of this variation is tentatively attributed to local inhomogeneities of the growth or patterning process, which could lead to small strain differences not detectable by XRD. Besides these findings, we underline the fact that SMR measurements performed for external magnetic fields smaller or comparable to the effective anisotropy fields allow for the accurate characterization of both the magnitude and direction of the magnetic anisotropy of YIG/Pt bilayers, with an accuracy better than 10 μ T.

YIG films with $t_{\text{YIG}} = 90 - 10$ nm present large, mm size, in-plane domains delimited by zigzag boundaries and Néel domain walls. The apices of the zigzags are pinned by defects, whereas the straight sections of the walls incorporate Bloch-like singularities, which separate regions of the walls with opposite magnetization chirality. The domain morphology changes abruptly in the thinner films. Whereas the 8.7 nm thick YIG presents elongated domains that are tens of μ m long, the domains in the 3.7 nm thick YIG are smaller and more irregular, consistent with the reduction of the easy-plane and uniaxial anisotropy reported for this sample. Our measurements indicate that the performance of YIG-based spintronic devices may be strongly influenced by the thickness as well as by local variations of the YIG magnetic properties.

ACKNOWLEDGMENTS

We thank Rolf Allenspach for valuable discussions. Furthermore, we acknowledge funding by the Swiss National Science Foundation under Grant no. 200020-172775. Jaianth Vijayakumar is supported by the Swiss National Science Foundation through Grant no. 200021-153540. David Bracher is supported by the Swiss Nanoscience Institute (Grant no. P1502). Part of this work was performed at the SIM beamline of the Swiss Light Source, Paul Scherrer Institut, Villigen, Switzerland.

-
- ¹ K.-i. Uchida, H. Adachi, T. Ota, H. Nakayama, S. Maekawa, and E. Saitoh, *Applied Physics Letters* **97**, 172505 (2010).
- ² M. Schreier, N. Roschewsky, E. Dobler, S. Meyer, H. Huebl, R. Gross, and S. T. Goennenwein, *Applied Physics Letters* **103**, 242404 (2013).
- ³ W. Wang, S. Wang, L. Zou, J. Cai, Z. Sun, and J. Sun, *Applied Physics Letters* **105**, 182403 (2014).
- ⁴ N. Vlietstra, J. Shan, B. Van Wees, M. Isasa, F. Casanova, and J. B. Youssef, *Physical Review B* **90**, 174436 (2014).
- ⁵ B. Heinrich, C. Burrowes, E. Montoya, B. Kardasz, E. Girt, Y.-Y. Song, Y. Sun, and M. Wu, *Physical Review Letters* **107**, 066604 (2011).
- ⁶ V. Castel, N. Vlietstra, B. Van Wees, and J. B. Youssef, *Physical Review B* **86**, 134419 (2012).
- ⁷ H. Wang, C. Du, Y. Pu, R. Adur, P. Hammel, and F. Yang, *Physical Review B* **88**, 100406 (2013).
- ⁸ V. Castel, N. Vlietstra, B. van Wees, and J. B. Youssef, *Physical Review B* **90**, 214434 (2014).
- ⁹ L. Cornelissen, J. Liu, R. Duine, J. B. Youssef, and B. Van Wees, *Nature Physics* **11**, 1022 (2015).
- ¹⁰ L. Cornelissen and B. van Wees, *Physical Review B* **93**, 020403 (2016).
- ¹¹ L. J. Cornelissen, K. J. Peters, G. E. Bauer, R. Duine, and B. J. van Wees, *Physical Review B* **94**, 014412 (2016).
- ¹² S. Emori, A. Matyushov, H.-M. Jeon, C. J. Babroski, T. Nan, A. M. Belkessam, J. G. Jones, M. E. McConney, G. J. Brown, B. M. Howe, *et al.*, *Applied Physics Letters* **112**, 182406 (2018).
- ¹³ J. Sklenar, W. Zhang, M. B. Jungfleisch, W. Jiang, H. Chang, J. E. Pearson, M. Wu, J. B. Ketterson, and A. Hoffmann, *Physical Review B* **92**, 174406 (2015).
- ¹⁴ H. Nakayama, M. Althammer, Y.-T. Chen, K. Uchida, Y. Kajiwara, D. Kikuchi, T. Ohtani, S. Geprags, M. Opel, S. Takahashi, *et al.*, *Physical Review Letters* **110**, 206601 (2013).
- ¹⁵ Y.-T. Chen, S. Takahashi, H. Nakayama, M. Althammer, S. T. Goennenwein, E. Saitoh, and G. E. Bauer, *Physical Review B* **87**, 144411 (2013).
- ¹⁶ C. Hahn, G. De Loubens, O. Klein, M. Viret, V. V. Naleto, and J. B. Youssef, *Physical Review B* **87**, 174417 (2013).
- ¹⁷ M. Althammer, S. Meyer, H. Nakayama, M. Schreier, S. Altmannshofer, M. Weiler, H. Huebl, S. Geprags, M. Opel, R. Gross, *et al.*, *Physical Review B* **87**, 224401 (2013).
- ¹⁸ N. Vlietstra, J. Shan, V. Castel, J. Ben Youssef, G. Bauer, and B. Van Wees, *Applied Physics Letters* **103**, 032401 (2013).
- ¹⁹ M. Schreier, T. Chiba, A. Niedermayr, J. Lotze, H. Huebl,

- S. Geprags, S. Takahashi, G. E. Bauer, R. Gross, and S. T. Goennenwein, *Physical Review B* **92**, 144411 (2015).
- ²⁰ Z. Fang, A. Mitra, A. Westerman, M. Ali, C. Ciccarelli, O. Cespedes, B. Hickey, and A. Ferguson, *Applied Physics Letters* **110**, 092403 (2017).
- ²¹ R. Pearson, in *Proceedings of the Seventh Conference on Magnetism and Magnetic Materials* (Springer, 1962) pp. 1236–1242.
- ²² P. Hansen, K. Enke, and G. Winkler, in *Part A: Garnets and Perovskites* (Springer, 1978) pp. 82–86.
- ²³ D. Heinz, P. Besser, J. Owens, J. Mee, and G. Pulliam, *Journal of Applied Physics* **42**, 1243 (1971).
- ²⁴ A. Thiaville, F. Boileau, J. Miltat, and L. Arnaud, *Journal of Applied Physics* **63**, 3153 (1988).
- ²⁵ F. V. Lisovskii, E. G. Mansvetova, M. P. Temiryazeva, and A. G. Temiryazev, *JETP Letters* **96**, 596 (2013).
- ²⁶ P. Pirro, T. Bracher, A. Chumak, B. Lagel, C. Dubs, O. Surzhenko, P. Gornert, B. Leven, and B. Hillebrands, *Applied Physics Letters* **104**, 012402 (2014).
- ²⁷ B. B. Krichevtsov, S. V. Gastev, S. M. Sutturin, V. V. Fedorov, A. M. Korovin, V. E. Bursian, A. G. Bانشchikov, M. P. Volkov, M. Tabuchi, and N. S. Sokolov, *Science and Technology of Advanced Materials* **18**, 351 (2017).
- ²⁸ H. Wang, C. Du, P. C. Hammel, and F. Yang, *Physical Review B* **89**, 134404 (2014).
- ²⁹ J. F. K. Cooper, C. J. Kinane, S. Langridge, M. Ali, B. J. Hickey, T. Niizeki, K. Uchida, E. Saitoh, H. Ambaye, and A. Glavic, *Physical Review B* **96**, 104404 (2017).
- ³⁰ P. Dorsey, S. Bushnell, R. Seed, and C. Vittoria, *Journal of Applied Physics* **74**, 1242 (1993).
- ³¹ S. A. Manuilov, S. Khartsev, and A. M. Grishin, *Journal of Applied Physics* **106**, 123917 (2009).
- ³² S. A. Manuilov and A. M. Grishin, *Journal of Applied Physics* **108**, 013902 (2010).
- ³³ Y. Sun, Y.-Y. Song, H. Chang, M. Kabatek, M. Jantz, W. Schneider, M. Wu, H. Schultheiss, and A. Hoffmann, *Applied Physics Letters* **101**, 152405 (2012).
- ³⁴ O. d’Allivy Kelly, A. Anane, R. Bernard, J. Ben Youssef, C. Hahn, A. H. Molpeceres, C. Carretero, E. Jacquet, C. Deranlot, P. Bortolotti, *et al.*, *Applied Physics Letters* **103**, 082408 (2013).
- ³⁵ M. Onbasli, A. Kehlberger, D. Kim, G. Jakob, M. Klaui, A. Chumak, B. Hillebrands, and C. Ross, *Applied Physics Letters Materials* **2**, 106102 (2014).
- ³⁶ N. Sokolov, V. Fedorov, A. Korovin, S. Sutturin, D. Baranov, S. Gastev, B. Krichevtsov, K. Y. Maksimova, A. Grunin, V. Bursian, *et al.*, *Journal of Applied Physics* **119**, 023903 (2016).
- ³⁷ C. Hauser, T. Richter, N. Homonnay, C. Eisenschmidt, M. Qaid, H. Deniz, D. Hesse, M. Sawicki, S. G. Ebbinghaus, and G. Schmidt, *Scientific Reports* **6**, 20827 (2016).
- ³⁸ E. Popova, N. Keller, F. Gendron, L. Thomas, M.-C. Branso, M. Guyot, M. Tessier, and S. Parkin, *Journal of Vacuum Science & Technology A: Vacuum, Surfaces, and Films* **19**, 2567 (2001).
- ³⁹ A. Mitra, O. Cespedes, Q. Ramasse, M. Ali, S. Marmion, M. Ward, R. Brydson, C. Kinane, J. Cooper, S. Langridge, *et al.*, *Scientific Reports* **7**, 11774 (2017).
- ⁴⁰ J. M. Gomez-Perez, S. Velez, L. McKenzie-Sell, M. Amado, J. Herrero-Martın, J. Lopez-Lopez, S. Blanco-Canosa, L. E. Hueso, A. Chuvilin, J. W. Robinson, *et al.*, arXiv preprint arXiv:1803.05545 (2018).
- ⁴¹ M. B. Jungfleisch, A. V. Chumak, A. Kehlberger, V. Lauer, D. H. Kim, M. C. Onbasli, C. A. Ross, M. Klaui, and B. Hillebrands, *Physical Review B* **91**, 134407 (2015).
- ⁴² M. Haertinger, C. H. Back, J. Lotze, M. Weiler, S. Geprags, H. Huebl, S. T. B. Goennenwein, and G. Woltersdorf, *Phys. Rev. B* **92**, 054437 (2015).
- ⁴³ A. Kehlberger, U. Ritzmann, D. Hinzke, E.-J. Guo, J. Cramer, G. Jakob, M. C. Onbasli, D. H. Kim, C. A. Ross, M. B. Jungfleisch, B. Hillebrands, U. Nowak, and M. Klaui, *Physical Review Letters* **115**, 096602 (2015).
- ⁴⁴ A. Temiryazev, M. Tikhomirova, and I. Fedorov, *Journal of magnetism and magnetic materials* **258**, 580 (2003).
- ⁴⁵ W. Xia, Y. Chun, S. Aizawa, K. Yanagisawa, K. M. Krishnan, D. Shindo, and A. Tonomura, *Journal of Applied Physics* **108**, 123919 (2010).
- ⁴⁶ S. Geller and M. Gilleo, *Journal of Physics and Chemistry of Solids* **3**, 30 (1957).
- ⁴⁷ H. Chang, T. Liu, D. Reifsnnyder Hickey, P. P. Janantha, K. A. Mkhoyan, and M. Wu, *Applied Physics Letters Materials* **5**, 126104 (2017).
- ⁴⁸ C. Colliex, T. Manoubi, and C. Ortiz, *Physical Review B* **44**, 11402 (1991).
- ⁴⁹ P. Hansen, P. Roschmann, and W. Tolksdorf, *Journal of Applied Physics* **45**, 2728 (1974).
- ⁵⁰ E. Popova, N. Keller, F. Gendron, M. Guyot, M.-C. Branso, Y. Dumond, and M. Tessier, *Journal of Applied Physics* **90**, 1422 (2001).
- ⁵¹ Y. Dumont, N. Keller, E. Popova, D. Schmool, S. Bhattacharya, B. Stahl, M. Tessier, and M. Guyot, *Journal of Applied Physics* **97**, 10G108 (2005).
- ⁵² K. Garello, I. M. Miron, C. O. Avci, F. Freimuth, Y. Mokrousov, S. Blugel, S. Auffret, O. Boulle, G. Gaudin, and P. Gambardella, *Nature Nanotechnology* **8**, 587 (2013).
- ⁵³ C. O. Avci, K. Garello, A. Ghosh, M. Gabureac, S. F. Alvarado, and P. Gambardella, *Nature Physics* **11**, 570 (2015).
- ⁵⁴ C. T. Wang, X. F. Liang, Y. Zhang, X. Liang, Y. P. Zhu, J. Qin, Y. Gao, B. Peng, N. X. Sun, and L. Bi, *Physical Review B* **96**, 224403 (2017).
- ⁵⁵ S.-K. Chung and M. W. Muller, *Journal of Magnetism and Magnetic Materials* **1**, 114 (1975).
- ⁵⁶ J. Basterfield, *Journal of Applied Physics* **39**, 5521 (1968).
- ⁵⁷ V. Vlasko-Vlasov, L. Dedukh, and V. Nikitenko, *Zh. Eksp. Teor. Fiz* **71**, 2291 (1976).
- ⁵⁸ V. Vlasko-Vlasov, L. Dedukh, and V. Nikitenko, *JETP* **38**, 184 (1974).
- ⁵⁹ V. Vlasko-Vlasov, L. Dedukh, and V. Nikitenko, *Physica Status Solidi (a)* **29**, 367 (1975).
- ⁶⁰ M. Labrune, J. Miltat, and M. Klman, *Journal of Applied Physics* **49**, 2013 (1978).
- ⁶¹ L. Le Guyader, A. Kleibert, A. F. Rodrıguez, S. El Mousaoui, A. Balan, M. Buzzi, J. Raabe, and F. Nolting, *Journal of Electron Spectroscopy and Related Phenomena* **185**, 371 (2012).
- ⁶² C. Favieres, J. Vergara, and V. Madurga, *Journal of Physics: Condensed Matter* **25**, 066002 (2013).
- ⁶³ S. Hamzaoui, M. Labrune, and I. Puchalska, *Applied Physics Letters* **45**, 1246 (1984).
- ⁶⁴ A. Hubert and R. Schafer, *Magnetic Domains: The Analysis of Magnetic Microstructures* (Springer Berlin Heidelberg, 2008).
- ⁶⁵ M. Freiser, *IBM Journal of Research and Development* **23**, 330 (1979).
- ⁶⁶ M. Labrune, S. Hamzaoui, and I. Puchalska, *Journal of Magnetism and Magnetic Materials* **27**, 323 (1982).